Volume 4
Number 6
21 March 2022
Pages 1485–1708

Nanoscale Advances

rsc.li/nanoscale-advances

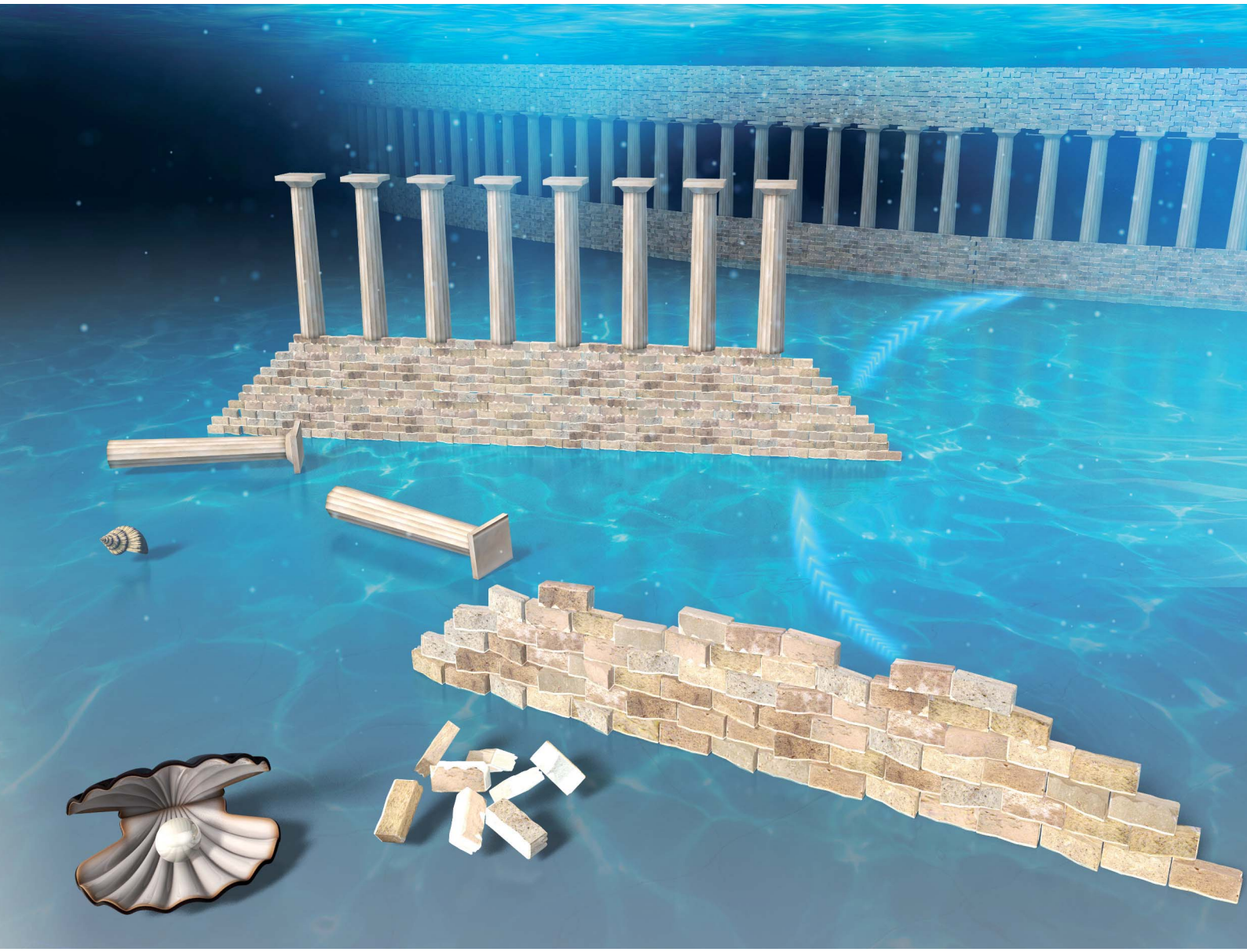

ISSN 2516-0230

ROYAL SOCIETY OF CHEMISTRY

PAPER

Hiroaki Imai *et al.*

Designed nanostructures created *via* physicochemical switching of the growth mode between single crystals and mesocrystals

NCNST

Nanoscale Advances

ROYAL SOCIETY OF CHEMISTRY

PAPER

View Article Online
View Journal | View Issue

Cite this: *Nanoscale Adv.*, 2022, **4**, 1538

Designed nanostructures created *via* physicochemical switching of the growth mode between single crystals and mesocrystals†

Sayako Kanazawa, Yuya Oaki and Hiroaki Imai *

Most biominerals are composed of mesocrystals, in which individual nanoparticle building units have a defined long-range order on the atomic scale in at least one direction. Although the crystal size and orientation of the mesostructures are spatially designed in biological architectures, it has been difficult to achieve adequate control of the crystal growth to produce modulated mesostructures in artificial aqueous systems. Here, we propose a simple physicochemical approach for the spatial design of nanostructures using an aqueous solution system. The ordered arrays of oriented fluorapatite (FA) rods similar to tooth enamel are produced on a polymer substrate in a supersaturated solution. We succeeded in reversible switching of the growth mode of FA between single-crystalline rods and mesocrystalline grains through the disturbance of the solution. The primary crystal size was tuned between micrometric rods ~0.5 μm wide and >5 μm long and nanoscale grains ~10 nm wide and 50 nm long without a drastic change in the *c* direction. Hierarchical architectures consisting of iso-oriented FA microrods and nanograins were constructed *via* temporal control of the crystal growth mode by switching a physicochemical parameter, such as the degree of supersaturation at the growth front.

Received 4th November 2021
Accepted 31st January 2022

DOI: 10.1039/d1na00784j

rsc.li/nanoscale-advances

Introduction

Biologically produced minerals have their own elaborate morphologies that have excellent mechanical and optical properties as compared with geologic bulky crystals.[1–8] In general, the hierarchical architectures of biominerals are composed of micrometric building blocks.[9,10] The detailed structures of calcium-based biominerals, such as seashells,[11] pearls,[12] eggshells,[13] coccoliths,[14,15] foraminifera,[16] corals,[17] bones,[18,19] and teeth,[20–22] have been studied as popular biological minerals.[9] For instance, the nacres of shells have a layered composite structure consisting of flat aragonite crystals and thin organic sheets.[23–25] The bones and teeth of vertebrates have a three-dimensional structure organized with hydroxyapatite (HA) nanocrystals and organic matrices.[26,27] The organic frames are important as a template and a control agent for biological mineralization processes. Various elaborate architectures have been reported to be constructed by the combination of soluble and insoluble biological organic agents in biotic aqueous systems.[28–31]

In recent years, various biominerals have been reported to consist of nanoscale units with the incorporation of organic polymers.[9,25] The assembly of nanoscale crystalline units that is observed in biominerals is not made of simple aggregates but is ordered in approximately the same crystallographic direction. The ordered arrangements of nanometric crystals are regarded as a mesocrystal, an intermediate structure between a homogeneous single crystal and a polycrystal, which is a random aggregate of small crystals.[32–35] In accordance with the modern definition,[36,37] a mesocrystal is delineated as a nanostructured material that consists of individual nanoparticle building units with a defined order on the atomic scale in at least one direction. The peculiar performance of biominerals originates from their hierarchical architectures that are comprised of nanograins aligned in specific directions.[9,38–43]

Mesocrystals are basically thought to be formed through particle-mediated self-assembly as a nonclassical crystallization process.[33,34] Rectangular nanoblocks, such as nanocubes and nanocuboids, are accumulated on a substrate by a lateral capillary force[44–48] at the vapor–liquid–solid interface and a depletion force between neighboring particles by the evaporation of a liquid medium.[49–52] Bridged-type mesocrystals[53–56] are produced by the self-organized growth of segmented crystalline units through an ion-mediated classical crystallization

Department of Applied Chemistry, Faculty of Science and Technology, Keio University, 3-14-1 Hiyoshi, Kohoku-ku, Yokohama 223-8522, Japan. E-mail: hiroaki@applc.keio.ac.jp

† Electronic supplementary information (ESI) available: The width and length of the grains in the films (Table S1); SEM images and XRD patterns of the original PVA sheet and the seed layer (Fig. S1); TEM image and SAED pattern of the films after growth in s-SBF1.0 (Fig. S2); SEM images and XRD pattern of the films after growth in s-SBF2.0 (Fig. S3); TEM image of grains obtained by fracturing the film after growth with stirring in s-SBF1.0 (Fig. S4); SEM images and XRD pattern of the films after growth with stirring in s-SBF2.0 (Fig. S5); SEM images of the films after growth at various ion concentrations (Fig. S6). See DOI: 10.1039/d1na00784j

process with the incorporation of organic and inorganic molecules. In any event, the formation of biogenic hierarchical structures forming the mesocrystal is associated with spatial and temporal control of the crystallization behavior. Here, the switching of the growth modes is essential for the elaborate design of the crystal architectures.

An aqueous solution containing inorganic ions nearly equal to those of human blood plasma, named simulated body fluid (SBF), has been utilized for the production of HA nanocrystals.[57–60] Sheets and needles of HA and fluorapatite (FA) crystals elongated along the *c*-axis have been produced in an SBF-based solution at human body temperature.[61] Enamel-mimetic films consisting of *c*-axis-oriented nanorods were fabricated using multistep crystal growth on a self-standing polyvinyl alcohol (PVA) sheet in a simplified SBF system.[57,62] The formation of oriented films with FA microrods was promoted through geometric selection in the presence of fluoride ions. The subsequent growth with D-aspartic acid produced an enamel-like structure consisting of oriented nanorods on basal microrods. The chemical conditions can be changed in each step. However, the controllability is not sufficient for the formation of hierarchically structured elaborate architectures.

In the present article, we propose a simple physicochemical approach for the spatial design of enamel-like mesostructures (Fig. 1). Ordered arrays similar to tooth enamel are produced by the oriented growth of FA rods on a PVA substrate in a supersaturated solution system (Fig. 1a and b). We found that reversible switching of the growth mode of FA rods was achieved by the disturbance of the solution (Fig. 1c and d). According to detailed characterization, the primary crystal-size units were revealed to be switched between micrometric rods and nanoscale grains with changing the degree of supersaturation. Finally, hierarchical architectures consisting of iso-oriented microrods and oriented nanograins were successfully constructed through temporal control of the crystal growth mode (Fig. 1d and e). Our findings provide novel technological insight into the fabrication of highly ordered architectures in artificial systems by mimicking biological mineralization systems.

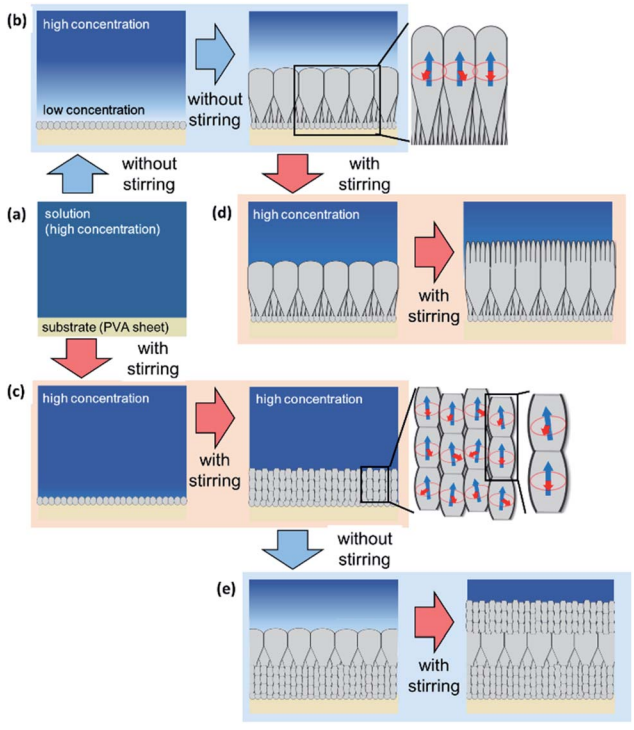

Fig. 1 Schematic illustrations of the growth modes of nanorods and nanograins under supersaturated conditions with and without stirring. The density of the blue color indicates the ion concentration. (a) The initial conditions and (b) growth behaviors without stirring, (c) with stirring, (d) with stirring after no stirring, and (e) repetition of without/with stirring. Blue and red arrows indicate the *c* and *a* directions, respectively.

Experimental section

Preparation of precursor solutions

Common SBF is a buffered mineralization solution containing various ions of human blood plasma.[59] In a previous study, we used an SBF-based solution (s-SBF1.0) simplified by the removal of minor ions, such as Mg^{2+}, SO_4^{2-}, and HCO_3^-.[57,61,62] s-SBF1.0 was prepared by mixing HCl (Junsei Chemical), $CaCl_2 \cdot 2H_2O$ (Junsei Chemical), Na_2HPO_4 (Junsei Chemical), and NaCl (Kanto Chemical) with purified water. The concentrations of Ca^{2+}, HPO_4^{2-}, Na^+, and Cl^- were 2.5, 1.0, 142.0, and 141.0 mmol dm^{-3}, respectively. The pH was adjusted to 7.2 by adding tris(hydroxymethyl)aminomethane (Junsei Chemical) to control the growth conditions of apatite crystals.

In the present work, we increased the ion concentrations in the supersaturated solutions to promote nucleation and regulate the growth rate (s-SBF*x*, x = 2.00, and 3.75). The ion concentrations in s-SBF*x* were x times higher than those in s-SBF. The concentration of fluoride ions was 1.50–2.25 mmol dm^{-3}. The solution was kept at 37 °C for 6–24 h. Deposition was performed in a 250 cm^3 closed polypropylene vessel (diameter: 60 mm). The nucleation of FA on a PVA sheet (Aisero Solublon® MA, saponification rate >99.5%, M_w: 1700, and 25 μm thick) supported on a polypropylene plate using masking tape was used as a substrate for the nucleation of apatite crystals. Commercially available PVA with a high saponification is insoluble in water below 40 °C. We used s-SBF3.75 at $[F^-]$ = 2.25 mmol dm^{-3} to promote heterogeneous nucleation on the PVA surface. The solution was kept at 37 °C for 6 h. The resulting products were washed with pure water at room temperature.

The growth medium was then changed to s-SBF1.0 at $[F^-]$ = 1.50 mmol dm^{-3} after washing with purified water to enhance the crystal growth on the seed layer. The solution was kept at 37 °C for 24 h with and without stirring. We stirred the solution with a magnetic stirrer and a stirring bar at 100–400 rpm. The concentrations of calcium and phosphate ions were varied from the standard values ($[Ca]^{2+}$: 2.5 mmol dm^{-3}; $[HPO_4^{2-}]$: 1.0 mmol dm^{-3}) to $[Ca]^{2+}$ = 0.5–1.25 and $[HPO_4^{2-}]$ = 0.5–2.0 mmol dm^{-3}, respectively, to change the width of the crystalline rods.

Characterization

The structures of the products were characterized using scanning electron microscopes (SEMs, JEOL JSM-7600F) and a field-emission transmission electron microscope (TEM, FEI Tecnai) equipped with energy-dispersive X-ray spectroscopy (EDX, Bruker Quantax). Thin platy samples ~100 nm thick were prepared using the focused ion beam (FIB) technique for TEM observation. The X-ray diffraction (XRD) patterns were recorded using a Bruker D8 Advance. The solution concentration before and after the reaction was measured using inductively coupled plasma atomic emission spectroscopy (ICP-AES, Shimadzu ICPE-9000).

Results and discussion

Formation of *c*-axis-oriented FA films without stirring

We prepared *c*-axis-oriented FA films using stepwise deposition on a PVA sheet according to our previous work.[57] In the initial step, a seed layer of FA was produced through heterogeneous nucleation in a highly supersaturated solution containing fluoride ions. Densely packed FA nanorods ~100 nm wide were deposited on the surface after reaction for several hours in s-SBF3.75 at $[F^-] = 2.25$ mmol dm^{-3} (Fig. S1 in the ESI†).

We produced FA films through subsequent growth on the seed layer after washing with purified water. The growth medium was changed to s-SBF1.0 at $[F^-] = 1.50$ mmol dm^{-3}. After being kept at 37 °C for 24 h without stirring, a film ~6 μm thick and consisting of nanorods was produced on the PVA surface (Fig. 2a). The width of the FA rods was ~300 nm at the upper part and ~100 nm at the elementary part (Table S1 in the ESI†). Because an intense 002 peak of FA was observed in the XRD pattern for the films (Fig. 2h), the nanorods comprise FA crystals that are elongated along the *c* axis. The radial growth of the nanorods from a nucleation point was partially observed in an enlarged image (Fig. 2c). Although crystal growth was restricted in the film, the rods normal to the surface survived through geometric selection. Consequently, we obtained FA films that consisted of *c*-axis-oriented nanorods arranged perpendicularly to the surface (Fig. 2a and b). A typical spot pattern of the selected area electron diffraction (SAED) pattern obtained from a TEM image of an FIB-cut plate indicates that a nanorod is a single crystal (Fig. S2 in the ESI†). The duplation of the solute concentrations (s-SBF2.0) led to an increase in the film thickness to ~10 μm without a change in the rod width (Fig. S3 in the ESI†).

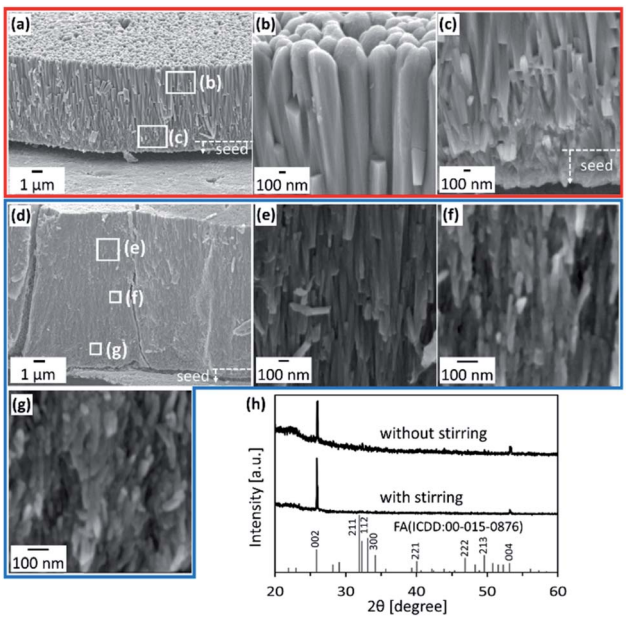

Fig. 2 SEM images (a–g) of the cross-sectional view and typical XRD patterns (h) of the films after subsequent growth in s-SBF1.0 at $[F^-] = 1.50$ mmol dm^{-3} for 24 h on the seed layer without (a–c in a red frame) and with stirring at 230 rpm (d–g in a blue frame).

Formation of *c*-axis-oriented FA films with stirring

As shown in Fig. 2d–g, we produced *c*-axis-oriented FA films through subsequent growth on the seed layer in s-SBF1.0 at $[F^-] = 1.50$ mmol dm^{-3} with stirring of the solution using a magnetic stirrer at 230 rpm. The films were found to consist of nanograins and nanorods smaller than those in the films produced without stirring (Fig. 2d). We observed nanograins ~30–80 nm wide and ~100–500 nm long (Fig. 2e–g). Table S1 in the ESI† shows detailed information of the grain width and length depending on the growth conditions and the position of the film. The presence of nanoscale grains was also confirmed from the TEM observation of fractured samples (Fig. S4 in the ESI†). Neither the deposition behavior nor the nanostructures were influenced by the stirring rate in a range of 100–400 rpm. An intense signal assigned to the 002 reflection in the XRD pattern (Fig. 2h) indicates that the FA nanograins and nanorods were arranged in approximately the *c* direction. Consequently, the FA crystals composing the films are deduced to be miniaturized with the disturbance of the solution. Here, the crystallographic direction of the units is maintained regardless of the size reduction. The nanograins were also observed in s-SBF2.0 at $[F^-] = 1.50$ mmol dm^{-3} with stirring of the solution (Fig. S5 in the ESI†). The duplation of the solute concentrations decreased the width and length of the nanograins (Table S1 in the ESI†).

Formation of layered architectures through multistep growth with and without stirring

We fabricated bilayer architectures that consisted of *c*-axis-oriented FA nanograins and nanorods on the seed layer with and without stirring of the solution. Fig. 3a and b show the SEM images of a bilayer film. In the first stage of the growth without stirring for 24 h, the lower layer consisting of nanorods ~100 nm wide at the root and ~500 nm wide at the top was formed on the seed surface (Fig. 3a). Nanorods longer than 5 μm were arranged perpendicularly to the surface through geometric selection. The upper layer consisting of FA nanorods ~30 nm wide was produced with stirring for 24 h (Fig. 3b and c). Here, the growth units are found to be suddenly miniaturized with the disturbance of the solution.

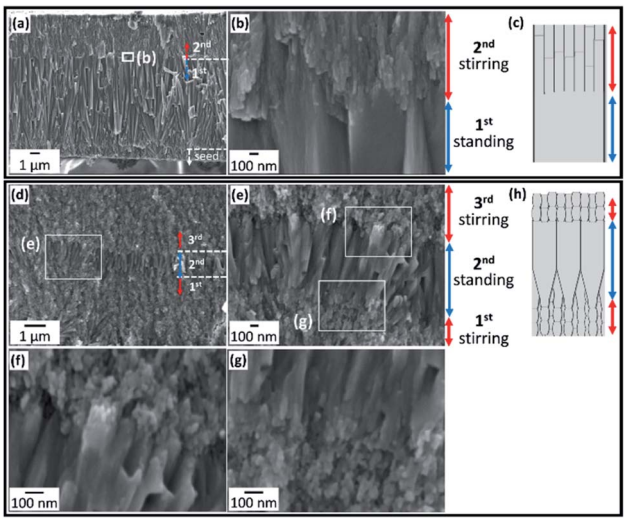

Fig. 3 SEM images (a, b and d–g) of the cross-sectional view and schematic illustrations (c and h) of the bilayer (a–c) and three-layer (d–h) films after subsequent growth in s-SBF2.0 at $[F^-] = 1.50$ mmol dm^{-3} without and with stirring.

As shown in Fig. 3d–h, three-layered architectures were fabricated on the seed by multistep growth with and without stirring. After the subsequent growth in s-SBF2.0 at $[F^-] = 1.50$ mmol dm^{-3} with stirring for 1 h, we suspended the stirring for 1 h and then resumed stirring. We observed nanograins ~20 nm wide and ~60 nm long in the first and third layers and nanorods ~80 nm wide and >600 nm long in the middle. Thus, the growth units expanded with the suspension of stirring and were then miniaturized when the disturbance of the solution resumed.

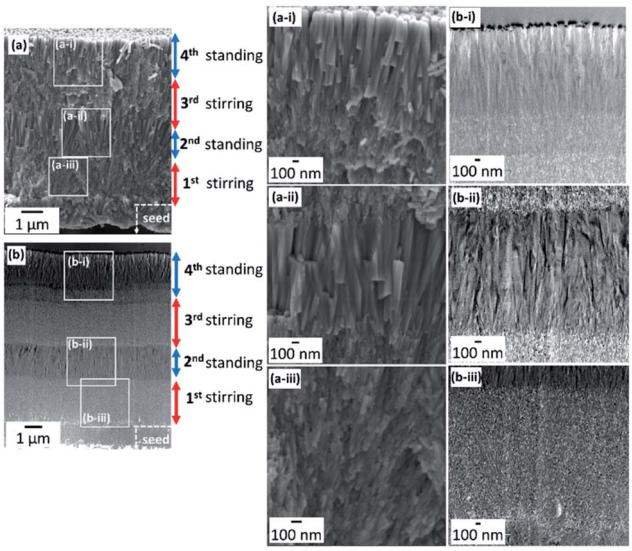

Fig. 4 SEM (a) and TEM (b) images showing a cross-sectional view of the four-layer films after subsequent growth in s-SBF1.0 at $[F^-] = 1.50$ mmol dm^{-3} without and with stirring. The TEM images were obtained from an FIB-cut sample.

Fig. 4 shows the cross-sectional SEM and TEM images of four-layered films. The TEM images were obtained from an FIB-cut sample. In the first stage of the growth with stirring for 1 h, the first layer, which consisted of FA nanograins ~20 nm wide, was formed on the seed surface (Fig. 4a-iii and b-iii). The second layer, which consisted of FA nanorods ~100 nm wide at the root and ~200 nm wide at the top, was grown for 5 h without stirring on the first layer (Fig. 4a-ii and b-ii). Nanorods >1 μm long in the second layer were arranged in almost the same direction, which was normal to the substrate. The third layer with stirring and the fourth one without stirring were composed of nanograins ~20 nm wide and nanorods ~100 nm wide, respectively (Fig. 4a-i and b-i).

As shown in Fig. 3 and 4, we succeeded in switching the growth mode between micrometric rods and nanometric grains by stirring. Here, we characterized the crystallographic direction of the nanograins and nanorods using the enlarged TEM images and SAED patterns of an FIB-cut sample (Fig. 5). Based on the SAED patterns, the nanorods are deduced to be elongated along the *c* axis (Fig. 5a and d). According to the spot pattern in the SAED images, the nanograins were deduced to be arranged in approximately the *c* direction, although the *a* axes of FA were randomly rotated around the *c* axis. The density constant in the TEM images indicates a slight variation of the crystallographic direction. Based on the given International

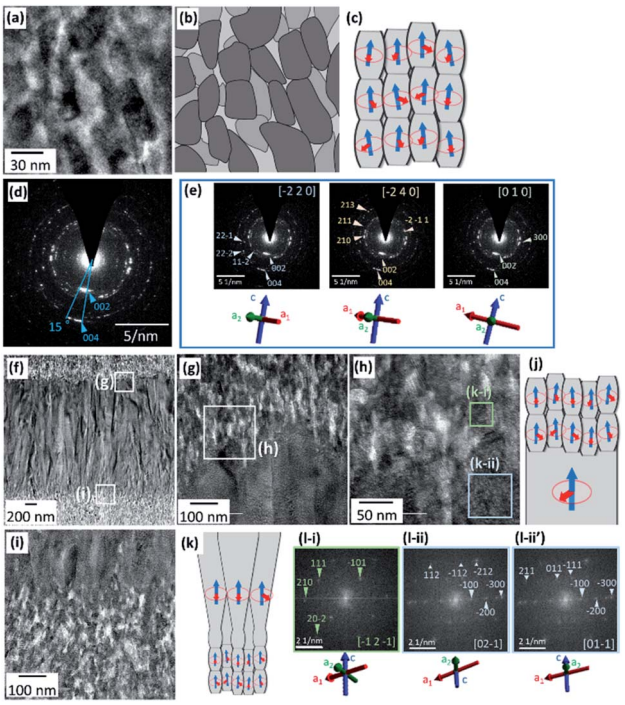

Fig. 5 TEM images (a and f–i) and schematic illustrations (b, c, j and k) of the FIB-cut plates of the film after subsequent growth in s-SBF1.0 at $[F^-] = 1.50$ mmol dm^{-3} on the seed layer. The granular structure obtained (a–c) with stirring for 3 h. SAED images (d and e) were obtained from (a). The layered structure obtained by repetition of with/without/with stirring (f–i). FFT images (l-i, l-ii, and l-ii′) were obtained from (h). Blue and red arrows indicate the *c* and *a* directions, respectively, in the schematic illustration.

Union of Crystallography definition of crystals, a distinct definition of a mesocrystal was proposed: "a nanostructured material with a defined long-range order on the atomic scale (in at least one direction), which can be inferred from the existence of an essentially sharp wide-angle diffraction pattern together with clear evidence that the material consists of individual nanoparticle building units".[37] The *c* axes of building units in the present mosaic structure are almost parallel (deviation ~15°), although their *a* direction is random. Therefore, we succeeded in fabricating mesocrystalline FA with stirring of the solution.

Fig. 5f–l show enlarged TEM images with fast Fourier transform (FFT) patterns at the interfaces between nanorods and nanograins. According to the FFT images (Fig. 5l-i, ii and ii′), the *c* directions are almost the same between the lower part and the upper small crystal. Thus, the nanograins were deduced to be stacked on the basal nanorods (Fig. 5f–h) in approximately the *c* direction. After the growth of nanorods, the disturbance miniaturizes the growth units and induces the formation of mesocrystals consisting of iso-oriented nanograins. Since the basal rod provided the spot pattern of the SAED image (Fig. S2 in the ESI†), the mesocrystal is produced on a single crystal.

We found that the nanorods were grown on the nanograins at the interface between the growth with and without stirring (Fig. 5i and k). Here, a nanograin grows a nanorod through expansion of the width with the suspension of stirring. Thus, the halt in the disturbance induces the gradual growth of FA crystals in the solution.

The influence of concentration on the crystal size

We succeeded in controlling the width of the FA crystals formed under the stirring conditions. Fig. 6 shows the variation in the width of FA crystals with a change in the concentration of the solution. When the product of the ion concentration of calcium and phosphate increased from 0.045 to 2.71 $(\text{mmol dm}^{-3})^2$, the width decreased from 120 to 20 nm (Fig. S6 in the ESI†). The crystal size is deduced to depend on the degree of supersaturation. Since the rods over 100 nm wide were produced even under the stirring conditions, the miniaturization is not simply attributed to the physical effect of disturbance. As shown in Fig. 3, the width of the FA nanograins increased from ~30 to ~80 nm with prolonging of the reaction time with stirring. The variation is ascribed to a decrease in the concentrations of calcium and phosphate ions with the growth of the crystal.

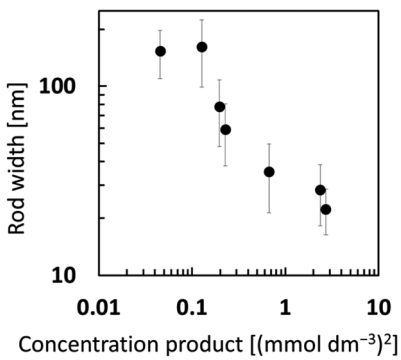

Fig. 6 The variation in the width of FA nanorods or nanograins with a change in the product of calcium and phosphate ion concentrations.

Nanorods are formed at a relatively low degree of supersaturation with the ion concentration gradient without stirring. Nanograins are then produced at a relatively high degree of supersaturation with stirring. Finally, we obtain periodic layered nanostructures by chaining the growth mode through the variation of the physicochemical conditions.

The mechanism of growth-mode switching

Fig. 1 illustrates the mechanism of growth-mode switching with and without stirring. In the initial stage, nucleation occurs densely on the substrate due to a high degree of supersaturation (Fig. 1a). When the ion diffusion rate is not sufficient under static conditions, the ion concentration at the growth front decreases gradually (Fig. 1b). The ion concentration gradient is then formed between the growth front and the bulk of the solution. The crystal gently grows at a relatively low degree of supersaturation. The preferential growth of FA occurs in the *c* direction. The rods are arranged perpendicularly to the substrate surface through geometric selection. Finally, crystalline thick rods elongated in the *c* direction are formed through the gentle growth mode.

When the solution is stirred, the ion concentration is homogenized in the solution (Fig. 1c). Thus, the ion concentration at the growth front is maintained for a certain period because the diffusion layer is not formed. Small crystal grains are formed at a relatively high degree of supersaturation (Fig. 1c). Here, the crystal structure of the nanograins is influenced by that of the basal crystal. The *c* axis of the upper crystals is inherited from that of the lower ones, while the *a* axis is randomly changed. Finally, we obtain mesocrystals, in which individual nanoparticle building units have a defined long-range order on the atomic scale in at least one direction.

The nanostructures are designed by switching the growth mode. The mesocrystals are produced on thick rods with an increase in the solute concentrations at the growth front by stirring the solution (Fig. 1d and e). Thick rods grow on the mesocrystals with a decrease in solute concentrations at the growth front by halting the stirring of the solution.

Conclusion

The reversible switching of the growth mode between single crystalline rods and mesocrystalline grains is achieved by the disturbance of the solution. Hierarchical architectures consisting of iso-oriented fluorapatite (FA) microrods and nanograins that were approximately arranged along the *c* direction were successfully designed through temporal control of the crystal growth mode. Ordered arrays similar to tooth enamel are produced by the oriented growth of FA rods in a supersaturated aqueous solution system. This method is regarded as a simple physicochemical approach to the spatial design of periodical nanostructures.

Conflicts of interest

There are no conflicts to declare.

Acknowledgements

This work was supported by JSPS KAKENHI grant number JP21H01627.

Notes and references

1 F. I. Alagboso, C. Reisecker, S. Hild and A. Ziegler, *J. Struct. Biol.*, 2014, **187**, 158–173.
2 K. Nakajima, Y. Nagai, M. Suzuki, Y. Oaki, K. Naito, Y. Tanaka, T. Toyofuku and H. Imai, *CrystEngComm*, 2016, **18**, 7135–7139.
3 D. Gur, B. A. Palmer, S. Weiner and L. Addadi, *Adv. Funct. Mater.*, 2017, **27**(1–13), 1603514.
4 Y. Ma, S. R. Cohen, L. Addadi and S. Weiner, *Adv. Mater.*, 2008, **20**, 1555–1559.
5 C. Merkel, J. Deuschle, E. Griesshaber, S. Enders, E. Steinhauser, R. Hochleitner, U. Brand and W. W. Schmahl, *J. Struct. Biol.*, 2009, **168**, 396–408.
6 M. E. Kunitake, L. M. Mangano, J. M. Peloquin, S. P. Baker and L. A. Estroff, *Acta Biomater.*, 2013, **9**, 5353–5359.
7 M. Rubner, *Nature*, 2003, **423**, 925–926.
8 G. Mayer, *Science*, 2005, **310**, 1144–1147.
9 Y. Oaki, A. Kotachi, T. Miura and H. Imai, *Adv. Funct. Mater.*, 2006, **16**, 1633–1639.
10 J. Aizenberg, J. C. Weaver, M. S. Thanawala, V. C. Sundar, D. E. Morse and P. Fratzl, *Science*, 2005, **309**, 275–278.
11 A. G. Checa, J. H. E. Cartwright and M. G. Willinger, *J. Struct. Biol.*, 2011, **176**, 330–339.
12 L. E. Murr and D. A. Ramirez, *J. Mineral.*, 2012, **64**, 469–474.
13 A. B. Rodríguez-Navarro, P. Marie, Y. Nys, M. T. Hincke and J. Gautron, *J. Struct. Biol.*, 2015, **190**, 291–303.
14 J. R. Young, S. A. Davis, P. R. Bown and S. Mann, *J. Struct. Biol.*, 1999, **126**, 195–215.
15 K. Simkiss and K. M. Wilbur, *Biomineralization*, Academic Press, San Diego, 1989.
16 S. Iwasaki, K. Kimoto, O. Sasaki, H. Kano, M. C. Honda and Y. Okazaki, *Paleoceanography*, 2015, **30**, 317–331.
17 M. Sugiura, K. Yasumoto, M. Iijima, Y. Oaki and H. Imai, *CrystEngComm*, 2021, **23**, 3693–3700.
18 H. P. Schwarcz, D. M. Binkley, L. Luo and K. Grandfield, *Bone*, 2020, **135**(1–13), 115305.
19 E. A. McNally, H. P. Schwarcz, G. A. Botton and A. L. Arsenault, *PLoS One*, 2012, **7**, 1–12.
20 P. Bodier-Houllé, P. Steuer, J. M. Meyer, L. Bigeard and F. J. G. Cuisinier, *Cell Tissue Res.*, 2000, **301**, 389–395.
21 J. Xue, A. V. Zavgorodniy, B. J. Kennedy, M. V. Swain and W. Li, *J. Microsc.*, 2013, **251**, 144–153.
22 C. D. Lynch, V. R. O'Sullivan, P. Dockery, C. T. McGillycuddy and A. J. Sloan, *J. Anat.*, 2010, **217**, 106–115.
23 H. Gao, B. Ji, I. L. Jäger, E. Arzt and P. Fratzl, *Proc. Natl. Acad. Sci. U. S. A.*, 2003, **100**, 5597–5600.
24 B. T. Kato, A. Sugawara and N. Hosoda, *Adv. Mater.*, 2002, **14**, 869–877.
25 X. Li, W. C. Chang, Y. J. Chao, R. Wang and M. Chang, *Nano Lett.*, 2004, **4**, 613–617.
26 E. Beniash, C. A. Stifler, C. Y. Sun, G. S. Jung, Z. Qin, M. J. Buehler and P. U. P. A. Gilbert, *Nat. Commun.*, 2019, **10**, 1–13.
27 L. H. He and M. V. Swain, *Appl. Phys. Lett.*, 2007, **90**, 2005–2008.
28 S. Von Euw, Q. Zhang, V. Manichev, N. Murali, J. Gross, L. C. Feldman, T. Gustafsson, C. Flach, R. Mendelsohn and P. G. Falkowski, *Science*, 2017, **356**, 933–938.
29 X. Xu, X. Chen and J. Li, *J. Mater. Chem. B*, 2020, **8**, 2199–2215.
30 T. Akazawa, M. Murata, J. Hino, F. Nagano, T. Shigyo, T. Nomura, H. Inano, K. Itabashi, T. Yamagishi, K. Nakamura, T. Takahashi, S. Iida and H. Kashiwazaki, *Appl. Surf. Sci.*, 2012, **262**, 51–55.
31 V. Sharma, A. Srinivasan, F. Nikolajeff and S. Kumar, *Acta Biomater.*, 2021, **120**, 20–37.
32 T. Wang, M. Antonietti and H. Cölfen, *Chem.–Eur. J.*, 2006, **12**, 5722–5730.
33 H. Cölfen and S. Mann, *Angew. Chem., Int. Ed.*, 2003, **42**, 2350–2365.
34 H. Cölfen and M. Antonietti, *Angew. Chem., Int. Ed.*, 2005, **44**, 5576–5591.
35 C. Jinguang and Q. Limin, *Sci. China: Chem.*, 2012, **55**, 2318–2326.
36 L. Bergström, E. V. Sturm née Rosseeva, G. Salazar-Alvarez and H. Cölfen, *Acc. Chem. Res.*, 2015, **48**, 1391–1402.
37 E. V. Sturm and H. Cölfen, *Chem. Soc. Rev.*, 2016, **45**, 5821–5833.
38 K. Sato, Y. Oaki, D. Takahashi, K. Toshima and H. Imai, *Chem.–Eur. J.*, 2015, **21**, 5034–5040.
39 Y. Politi, T. Arad, E. Klein, S. Weiner and L. Addadi, *Science*, 2004, **306**, 1161–1164.
40 A. Berman, J. Hanson, L. Leiserowitz, T. F. Koetzle, L. Weiner and L. Addai, *Science*, 1993, **259**, 776–779.
41 A. Berman, L. Addadi and S. Weiner, *Nature*, 1988, **331**, 546–548.
42 S. Weiner and L. Addadi, *J. Mater. Chem.*, 1997, **7**, 689–702.
43 F. Nudelman, H. H. Chen, H. A. Goldberg, S. Weiner and L. Addadi, *Faraday Discuss.*, 2007, **136**, 9–25.
44 Y. Hagiwara, Y. Oaki and H. Imai, *Nanoscale*, 2021, **13**, 9698–9705.
45 A. Singh, R. D. Gunning, S. Ahmed, C. A. Barrett, N. J. English, J. A. Garate and K. M. Ryan, *J. Mater. Chem.*, 2012, **22**, 1562–1569.
46 A. V. Titov and P. Král, *Nano Lett.*, 2008, **8**, 3605–3612.
47 J. Brunner, I. A. Baburin, S. Sturm, K. Kvashnina, A. Rossberg, T. Pietsch, S. Andreev, E. Sturm (née Rosseeva) and H. Cölfen, *Adv. Mater. Interfaces*, 2017, **4**, 1–9.
48 M. Agthe, E. Wetterskog, J. Mouzon, G. Salazar-Alvarez and L. Bergström, *CrystEngComm*, 2014, **16**, 1443–1450.
49 T. Hiraide, H. Kageyama, Y. Nakagawa, Y. Oaki and H. Imai, *Chem. Commun.*, 2016, **52**, 7545–7548.

50 R. Matsumoto, Y. Nakagawa, H. Kageyama, Y. Oaki and H. Imai, *CrystEngComm*, 2016, **18**, 6138–6142.
51 Y. Nakagawa, H. Kageyama, Y. Oaki and H. Imai, *Langmuir*, 2015, **31**, 6197–6201.
52 Y. Nakagawa, H. Kageyama, Y. Oaki and H. Imai, *J. Am. Chem. Soc.*, 2014, **136**, 3716–3719.
53 Y. Oaki and H. Imai, *Angew. Chem., Int. Ed.*, 2005, **44**, 6571–6575.
54 H. Imai, Y. Oaki and A. Kotachi, *Bull. Chem. Soc. Jpn.*, 2006, **79**, 1834–1851.
55 H. Imai, T. Terada and S. Yamabi, *Chem. Commun.*, 2003, 484–485.
56 Y. Oaki, S. Hayashi and H. Imai, *Chem. Commun.*, 2007, 2841–2843.
57 K. Nakamura, Y. Oaki and H. Imai, *CrystEngComm*, 2017, **19**, 669–674.
58 T. Kokubo and S. Ito, *J. Biomed. Mater. Res.*, 1990, **24**, 331–343.
59 T. Kokubo and H. Takadama, *Biomaterials*, 2006, **27**, 2907–2915.
60 H. M. Kim, K. Kishimoto, F. Miyaji, T. Kokubo, T. Yao, Y. Suetsugu, J. Tanaka and T. Nakamura, *J. Biomed. Mater. Res.*, 1999, **46**, 228–235.
61 T. Kobayashi, S. Ono, S. Hirakura, Y. Oaki and H. Imai, *CrystEngComm*, 2012, **14**, 1143–1149.
62 K. Aita, Y. Oaki, C. Ohtsuki and H. Imai, *CrystEngComm*, 2015, **17**, 5551–5555.